Materials Today Advances 23 (2024) 100522

Contents lists available at ScienceDirect

Materials Today Advances

journal homepage: www.journals.elsevier.com/materials-today-advances/

Unraveling the role of relaxation and rejuvenation on the structure and deformation behavior of the Zr-based bulk metallic glass Vit105

Lucas M. Ruschel [a,*], Sergej Jakovlev [a], Oliver Gross [b], Nico Neuber [a], Bastian Adam [a], Maximilian Frey [a], Benedikt Schmidt [a], Benedikt Bochtler [b], Ralf Busch [a]

[a] Chair of Metallic Materials, Saarland University, 66123, Saarbrücken, Germany
[b] Amorphous Metal Solutions GmbH, 66424, Homburg, Germany

ARTICLE INFO

Keywords:
Bulk metallic glass
Vit105
Relaxation
Rejuvenation
Mechanical properties
Fictive temperature
Structure
Watch component

ABSTRACT

The influence of relaxation and rejuvenation on the deformation behavior of the Zr-based bulk metallic glass Vit105 ($Zr_{52.5}Cu_{17.9}Ni_{14.6}Al_{10}Ti_5$) was investigated, where a well-defined thermal history was systematically introduced by thermal treatments. Samples with a progressively lower fictive temperature exhibit a lower enthalpic state, coupled with a reduced degree of free volume, which is responsible for a continuous embrittlement observed in three-point beam bending tests. The generated database allows an assessment of the mechanical behavior of any amorphous component made of Vit105 by simple calorimetric measurements and the determination of the fictive temperature, which is of special interest for complex parts that cannot be easily evaluated in mechanical tests. Diffraction experiments with high energy synchrotron X-ray radiation reveal a correlation between the increase in rigid 3-atom cluster connections with the reduction in the fracture strain, as a measure of ductility, indicating a strong correlation with the thermal history. While the atomic connections seem to have a crucial contribution to the ductility, changes of the short- and medium-range order seem to be equally important. The current findings provide fundamental insights into the role of thermal history in metallic glass forming alloy systems and how it can be used to manipulate the structure and tailor their mechanical properties specifically to the needs of each application.

1. Introduction

Metallic glasses were first discovered in the Au–Si system in 1960 by Duwez et al. [1]. Since then, amorphous metals have attracted wide interest as a new branch of glass-forming materials due to their unique physical and chemical properties [2]. In the early days of this class of materials, extremely high cooling rates of around 10^6 Ks^{-1} were required to suppress crystallization and freeze-in the amorphous structure. This limited the component size to only thin films and ribbons with thicknesses in the range of a few micrometers, whereas the continuous alloy development in the following decades resulted in an increase of the critical casting size d_c to 1 mm and above in various systems [3–7]. This development towards bulk metallic glasses (BMGs, $d_c \geq 1$ mm) led to a decline in the required cooling rates for glass formation to around 100 Ks^{-1} (or even lower for the best glass formers), which enabled technological upscaling and commercialization [2,8]. One of the best and most well-known representatives in the Zr-based alloy family is $Zr_{52.5}Cu_{17.9}Ni_{14.6}Al_{10}Ti_5$ (in at%) or better known by its commercial name Vit105. This composition was developed at the California Institute of Technology in 1997 and is one of the best Zr-based glass-forming alloys in general [9]. Apart from its high glass-forming ability (GFA), which results in an excellent processability, Vit105 exhibits superior mechanical properties such as a high strength combined with a high hardness as well as a high elastic deformation limit [8,10,11].

The mechanical properties in conventional polycrystalline metals are mainly defined by the long-range periodic order of the lattice and its defects such as dislocations and grain boundaries. Amorphous metals, on the other hand, have no long-range order but ordering on the short- and medium-range length scale without the presence of these well-known defects and related classical deformation mechanisms [12]. According to the current state of the art, deformation in amorphous metals by shear bands is mainly triggered by the formation of shear transformation zones (STZs) in areas of increased free volume, which is predetermined by the frozen-in amorphous structure [13]. This means

* Corresponding author.
E-mail address: lucas.ruschel@uni-saarland.de (L.M. Ruschel).

https://doi.org/10.1016/j.mtadv.2024.100522
Received 14 June 2024; Received in revised form 30 July 2024; Accepted 1 August 2024
Available online 9 August 2024

that the properties of BMGs are not only defined by their chemical composition but also by their degree of relaxation, which is influenced by the processing conditions. One way to describe the different structural states of metallic glasses and the accompanying differences in mechanical performance is by means of the fictive temperature T_f [14–16]. This temperature marks the point at which the supercooled liquid deviates from its metastable equilibrium state. As the temperature of vitrification is well-defined by the fictive temperature, each T_f corresponds to a specific structural state with a consistent set of properties [17]. A higher fictive temperature is reflected in a larger degree of free volume, which facilitates the formation of STZs and thus shear bands, leading to improved ductility [14,18]. Since BMGs are in a non-equilibrium state, the system seeks to relax toward its thermodynamic equilibrium, which can be simply induced by annealing. This usually results in a degradation of the desired properties, such as fracture toughness or total fracture strain [19–22]. On the other hand, it is much more difficult to reverse structural relaxation in order to change the structure of metallic glasses in such a way that an increase of free volume is achieved [23]. Therefore, there is a high demand to identify suitable methods that can incorporate a defined amount of free volume/enthalpy into the system. A variety of approaches have been established such as cold rolling [24,25], high pressure torsion [26–31], irradiation [32,33], cryogenic cycling [34–39] and thermal annealing [40–43].

The present work focuses on the bulk glass forming alloy Vit105, featuring outstanding castability as well as high plasticity in as-cast conditions. This allows to introduce a progressive embrittlement as a function of the fictive temperature to systematically study the mechanical properties for a wide range of relaxation states. The evolution in fracture strain is discussed in terms of the internal enthalpy difference of various relaxation and rejuvenation states, resembling differences in their excess free volume. To achieve rejuvenation, the focus lied on the simplest post-processing method of thermal annealing in the supercooled liquid region followed by water quenching to freeze-in a high fictive temperature. This systematic analysis allows to predict the properties of amorphous parts based on their intrinsic enthalpic state, as was exemplarily done for a watch component that cannot be tested easily in mechanical tests due to its complex shape. Furthermore, the structural changes induced by the annealing procedures were determined in synchrotron diffraction studies and correlated with the alterations in ductility, providing valuable insights into structure–property correlations in metallic glasses.

2. Experimental procedure

2.1. Sample production of the amorphous feedstock material

The raw elements Zr (99.99 wt%), Cu (99.99 wt%), Ni (99.99 wt%), Al (99.99 wt%) and Ti (99.995 wt%) were used to synthesize the master alloy by fusing them together in an electric arc furnace under Ti-gettered high purity argon atmosphere. To ensure an even distribution of the elements, the ingots were flipped and remelted at least four times. After homogenization, the master alloys were cast in water-cooled Cu molds in the shape of beams measuring 2 mm × 3 mm × 50 mm (height × width × length) in a custom-built suction casting machine using the electric arc technology. The watch component of a 'bezel' was produced by the company Amorphous Metal Solutions GmbH (AMS) in Germany [44]. AMS uses a die-casting process specifically designed to cast amorphous metals, which is well suited for the processing of BMG components with complex geometries.

2.2. Annealing experiments

The annealing experiments were conducted in a Linkam THMS600 furnace, consisting of a heated silver block with high temperature control precision. The experiments were performed under high purity argon atmosphere to minimize oxidation. However, slight oxidation of the surface layer was unavoidable and therefore removed by sanding prior to mechanical testing and further analysis. The isothermal transition time τ from the glassy state into the supercooled liquid as a function of temperature were taken from Ref. [45], allowing to estimate the time the Vit105 system requires to relax towards the metastable equilibrium. To ensure relaxation into the equilibrium liquid, all isothermal annealing times at each temperature were performed for double the transition time τ. This guarantees equilibration, as the system cannot move to a deeper enthalpic state than the supercooled equilibrium liquid, if crystallization is excluded. Subsequent cooling leads to immediate vitrification due to the long relaxation times for annealing temperatures below the glass transition temperature T_g. Therefore, the annealing temperature corresponds to the new fictive temperature ($T_a = T_f$), which is also shown later in the 'Results' section. The relaxation protocols (1–7) are summarized in the low-temperature time-temperature-transformation diagram in Fig. 1a. Next to these relaxation experiments to set a well-defined T_f, annealed specimens according to protocol no. 5 (T_a = 641 K) were additionally heat treated in the supercooled liquid at 713 K for 30 s with subsequent water quenching (rejuvenation protocol no. 8) with the aim to restore a high fictive temperature with improved ductility. Rejuvenation at higher temperatures was not performed as the fast crystallization times for Vit105 do not allow proper temperature equilibration. Furthermore, continuous cooling experiments were performed with different cooling rates as shown in Fig. 1b. In this way, it is

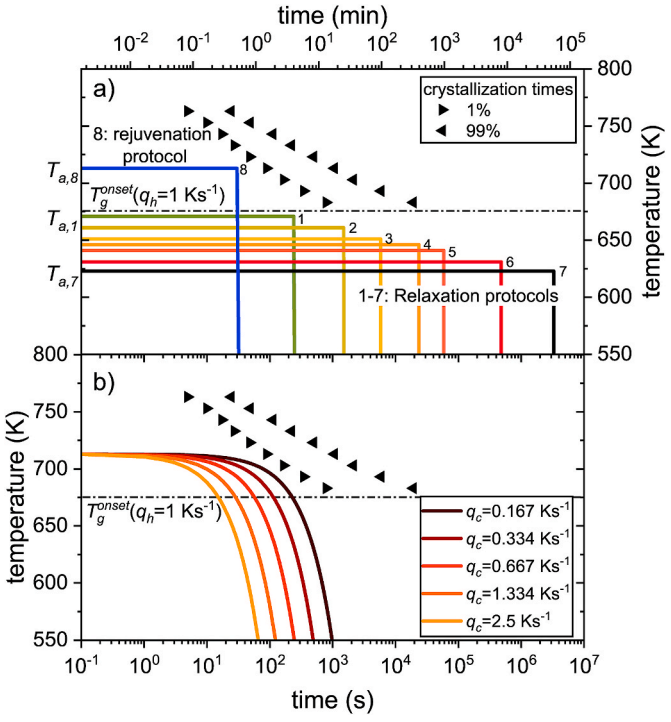

Fig. 1. a) Low temperature isothermal time-temperature-transformation diagram, representing the isothermal annealing protocols used in this study. All samples were heated with a rate of 2 Ks^{-1} to the desired annealing temperature. The curves 1 to 7 represent the isothermal annealing experiments for times longer than the transition times to establish a well-defined fictive temperature T_f (since $t > \tau_{trans}$: $T_{a,i} = T_{f,i}$, i = 1,2 …, 7)). The blue curve (8) represents the rejuvenation protocol, which starts with a synthetic embrittlement according to procedure (5), followed by heating into the supercooled liquid region at 713 K for 30 s (crystallization time of 89 s at this temperature) with subsequent water quenching to freeze in a fictive temperature that is as high as possible. b) Starting in the supercooled liquid at 713 K, continuous cooling experiments were carried out using various rates. The corresponding fictive temperature is then determined from calorimetric measurements by applying the Moynihan method [17].

possible to determine the fictive temperature of vitrification at a given cooling rate. This allows the estimation of an equivalent cooling rate for the different T_f set by isothermal annealing.

2.3. Mechanical testing

Three-point beam bending (3PBB) testing was performed for Vit105 samples with different fictive temperatures under ambient conditions. Rectangular shaped beams with nominal dimensions of 2 × 3 × 25 mm^3 (height h × width w × length L) were used, while the support distance was set to 20 mm. For statistical reasons, a set of 5 beams was tested for each T_f and the amorphous structure of each beam was verified by X-ray diffraction and calorimetric analysis. The tests were conducted on plane-parallel samples ground with 1200 grit paper using a displacement rate of 0.3 mm min^{-1} (=midpoint strain rate of 1.5 × 10^{-4} s^{-1} for the given nominal dimensions). The applied force F and deflection D were continuously measured to calculate the engineering stress σ and strain ε at the outer midpoint fiber of the beams according to:

$$\sigma = \frac{3FL}{2wh^2} \quad (1)$$

and

$$\varepsilon = \frac{6Dh}{L^2} \quad (2)$$

with the width w and height h of the beam.

2.4. Differential scanning calorimetry (DSC)

Thermal analyses were performed from 323 K to 853 K at heating rates of 1 Ks^{-1} under a constant high-purity argon flow (Ar. 99.999 vol %) in a Perkin Elmer DSC8000 using Al crucibles. The method of Moynihan was applied to determine the fictive temperature of the as-cast and annealed samples [17]. The DSC specimens were taken right next to the fracture surface of each beam (5 samples in total for each state), yielding good statistics for the determination of T_f.

2.5. Structural characterization by high-energy synchrotron X-ray diffraction

High-energy synchrotron X-ray diffraction (HEXRD) experiments were conducted in a transmission setup at the P21.2 beamline facility of PETRA III of the 'Deutsches Elektronensynchrotron' (DESY). The diffraction experiments of the as-cast and annealed specimens were performed from room temperature up to crystallization (heating rate of 0.33 Ks^{-1}) using the same Linkam THMS600 furnace as described in section 2.2. The beam size and energy were set to 500 μm × 500 μm and 68 keV (wavelength λ = 0.18233 Å), respectively. The HEXRD patterns were recorded with a VAREX XRD4343CT detector (2880 × 2880 pixels) with a pixel size of 150 μm × 150 μm and an exposure time of 5 s. The two-dimensional diffraction patterns were azimuthally integrated using PyFAI [46] and then baseline corrected using the PDFgetX2 software package [47] to obtain the structure factor S(Q) and reduced pair distribution function (PDF) G(r). More details can be found in our prior studies [48,49].

3. Results

3.1. The correlation of T_f with the enthalpic state and the cooling rate

As-cast Vit105 beams were aged according to Fig. 1a at various annealing temperatures T_a for certain times. In order to verify that the annealing temperature was sufficiently long to set a well-defined fictive temperature T_f, the Moynihan area matching method [17] was applied to the DSC measurements shown in Fig. 2a. The results are summarized in Table 1. The as-quenched specimens were determined to exhibit a high fictive temperature of 727 K due to the high cooling rate during copper mold casting. Additionally, it could be shown for the isothermal experiments that the annealing temperature closely matches the fictive temperature, even for the rejuvenated state despite a fast transition time of just 0.5 s at 713 K [45]. To exclude crystallization, the annealing times (2-times the transition time τ) were oriented at the low temperature isothermal crystallization times (see Fig. 1a) [45]. These were measured at temperatures close to the calorimetric glass transition temperature, however no crystallization times were available well below T_g due to the very slow crystallization kinetics. Since conventional X-ray diffraction is limited to resolve nano-crystallization [50], calorimetric measurements were performed, as small changes within the sample volume induce a reduction in the absolute crystallization enthalpy release ΔH_x. Therefore, ΔH_x was determined for each state to exclude crystallization and yield information about the amorphous fraction as given in Table 1. ΔH_x of the as-cast state was used as reference, revealing that the produced aging states from as-cast to T_f = 631 K remain fully amorphous after the relaxation and rejuvenation treatments. However, annealing at 623 K marks the low temperature limit for the thermal treatment, as the amorphous fraction was slightly reduced to ~91 % due to the first appearance of crystals ($\Delta H_x^{Ta=623\,K}$=0.91 $\Delta H_x^{as\text{-}cast}$). This is supported by the shift of the crystallization temperature T_x^{onset} to lower temperatures

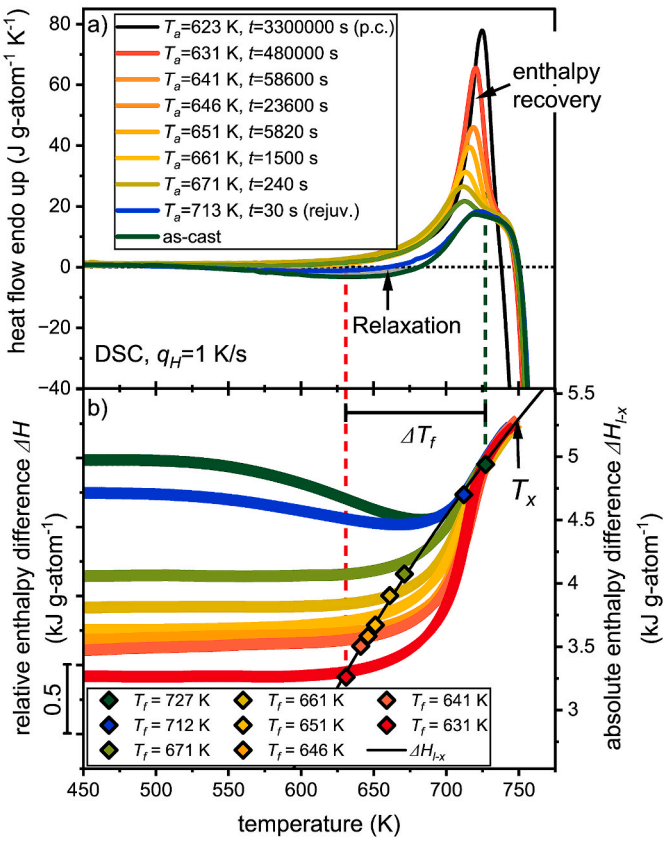

Fig. 2. a) DSC scans of Vit105 of the as-cast, rejuvenated and relaxed states. The latter were aged according to the transition times at the respective annealing temperature to achieve relaxation to the supercooled liquid state on long timescales. The deepest annealing temperature partially crystallized (p.c., black curve), which can be seen from the earlier onset for crystallization. The grey area below the dotted zero line represents the structural relaxation that occurs upon heating, while the overshoot during the glass transition represents the enthalpy recovery. b) The relative enthalpy difference curves are obtained by integration of the DSC curves (T_a = 623 K from a) is excluded due to partial crystallization). The curves are additionally pinned to the supercooled liquid region, as the enthalpy difference must be zero in the equilibrium state. The absolute enthalpy difference $\Delta H_{l\text{-}x}$ with respect to the crystalline mixture can be obtained from specific heat capacity measurements (details in the SI).

Table 1
Overview of the annealing temperatures and corresponding transition times. The fictive temperature T_f was determined with the Moynihan area matching method, revealing that T_f corresponds to the annealing temperature. Additionally, T_f was correlated to an equivalent cooling rate. The deepest annealing temperature probed (T_a = 623 K) indicates the lower temperature boundary for annealing in our chosen setup, as minor crystallization already occurred. This can be quantified by calculating the amorphous fraction ($\Delta H_x(T_a)/\Delta H_x(as\text{-}cast)$) from the crystallization enthalpy ΔH_x for each production state. The error bars correspond to the standard deviation of five measurements of each production state.

Annealing temperature T_a (K)	Transition time τ (s)	Annealing time (=2 × τ) (h)	Fictive temperature T_f (K)	Estimated cooling rate (Ks^{-1})[b]	Crystallization enthalpy ΔH_x (kJ g-atom^{-1})	Amorphous fraction (%)
– (As-cast)	–	–	727 ± 3	437	−3.42 ± 0.03	100
713 (Rejuvenation)	0.5	0.0083[a]	712 ± 1	84	−3.43 ± 0.04	100
671	120	0.066	671 ± 1	0.9	−3.43 ± 0.02	100
661	750	0.42	662 ± 1	0.3	−3.44 ± 0.04	100
651	2900	1.61	653 ± 1	0.1	−3.44 ± 0.03	100
646	12000	6.66	645 ± 1	0.05	−3.40 ± 0.03	100
641	29000	16.11	640 ± 3	0.03	−3.41 ± 0.03	100
631	240000	133	631 ± 2	0.01	−3.44 ± 0.02	100
623	1650000	917	–	–	−3.10 ± 0.04	91

[a] Annealing time>2 × τ to guarantee temperature equilibration.
[b] Based on Equation 3.

(black curve of Fig. 2a) compared to all the other states. Therefore, this partially crystalline state is excluded from further analysis.

Integration of the DSC scans against the crystalline baseline (which corresponds to the zero line) lead to enthalpy curves that yield information about the relative enthalpy difference between each state, as shown in Fig. 2b. The absolute enthalpy difference with respect to the crystalline state $\Delta H_{l\text{-}x}$ can be obtained by correlating the relative enthalpy difference at each fictive temperature to the absolute enthalpy difference. The latter can be obtained from specific heat capacity measurements of the Vit105 composition [45]. Comprehensive details about the correlation procedure to obtain the $\Delta H_{l\text{-}x}$ curves are provided in the supplementary information (SI). The enthalpy differences range from about 5 kJ g-atom^{-1} for the as-cast state to 3.25 kJ g-atom^{-1} for the annealed state of T_f = 631 K, i.e. the investigated states differ in their enthalpy, resembling their degree of relaxation, by up to 1.75 kJ g-atom^{-1} from each other. In the case of the rejuvenation protocol (8), the enthalpy was increased from 3.5 kJ g-atom^{-1} (=enthalpic state of T_f = 641 K) to 4.7 kJ g-atom^{-1}. The deviation of the enthalpy curves from the supercooled liquid line $\Delta H_{l\text{-}x}$ in the vicinity of the glass transition temperature results from the enthalpy recovery overshoot, where atomic mobility is regained, enabling the glassy structure to transition from its frozen state to the supercooled liquid. As visible in Fig. 2a, the enthalpy recovery becomes more pronounced with decreasing annealing temperature, since the structural rearrangements are kinetically constrained. This is caused by the progressively slower intrinsic time scales relative to the 'fast' heating rate in the DSC, leading to a lag in the enthalpy response to the new temperature conditions.

Furthermore, structural relaxation upon re-heating is only observed for the as-cast and rejuvenation specimens (see Fig. 2a), since the applied heating rate in the DSC is slower than the cooling rate during vitrification. In contrast, if the cooling rate during vitrification is slower than the applied heating rate in the DSC, no structural relaxation can be observed as visible for all aging states. This is attributable to the fact that the corresponding relaxation processes have already taken place during the annealing procedure. Since the cooling rate of each annealing state is not directly accessible from isothermal experiments, continuous cooling experiments were carried out at different rates (see Fig. 1b) to assign to each fictive temperature a cooling rate that results in an equivalent enthalpic state. The slower the cooling rate, the deeper the system can relax before vitrification, i.e. the liquid vitrifies at a lower fictive temperature. T_f was determined using the area matching method and is shown as a function of the applied cooling rate in the semi-log plot in Fig. 3. Despite the high cooling rate of 2.5 Ks^{-1} (the fastest cooling rate that can be used with the Linkam furnace), the melt stays in equilibrium for around 30 K due to the fast relaxation time above the calorimetric glass transition, until the system finally vitrifies at T_f = 682 K. With the slowest cooling rate of 0.167 Ks^{-1}, the system can relax to much lower temperatures (T_f = 659 K) before the system finally leaves the equilibrium liquid and forms a glass. The dependence follows a linear equation with a high R^2 value of 0.97, allowing the cooling rate q_c for different T_f to be estimated based on the following fit:

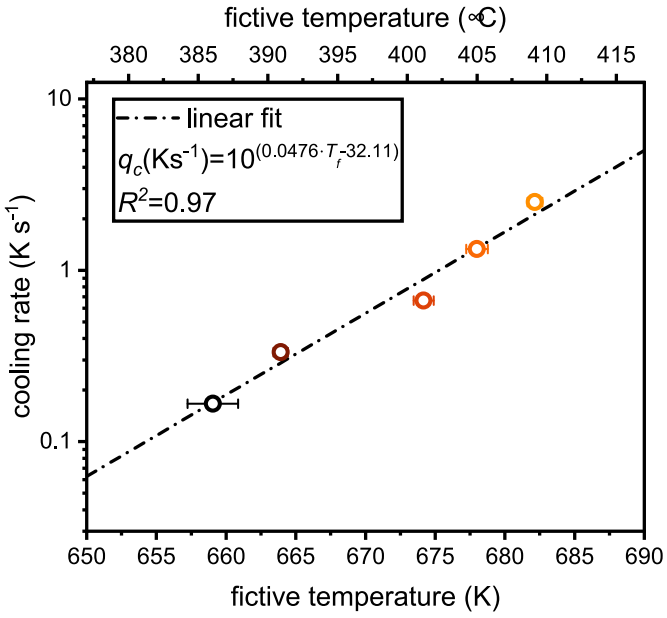

Fig. 3. Semi-log plot of cooling rate as a function of the fictive temperature. The fictive temperature was determined from DSC scans by applying the Moynihan method.

$$q_c\left(Ks^{-1}\right) = 10^{\left(0.0476\cdot T_f - 32.11\right)} \quad (3)$$

Detailed information of all important parameters, including the annealing temperatures, transition and annealing times, crystallization enthalpies and estimated cooling rate for each T_f can be found in Table 1.

3.2. Mechanical properties as a function of T_f

For application-oriented alloys such as Vit105, it is particularly important to understand the mechanical properties and their evolution with respect to the fictive temperature, as a low T_f significantly alters the ductility of an alloy [14]. A certain degree of ductility is particularly important to prohibit sudden failure, if the applied load unexpectedly

exceeds the yield strength. Fig. 4 shows engineering stress-strain curves for several fictive temperatures of Vit105, from deeply annealed through the rejuvenated state up to the as-cast condition. The as-cast beams with a high T_f of 727 K exhibit the largest ductility region in 3PBB experiments with a bending strain to failure of 6.50 %. The stepwise reduction of T_f led to a continuous decrease in ductility with a significant reduction at T_f of 631 K with almost no plasticity left, indicating that this fictive temperature is approaching the critical fictive temperature for embrittlement proposed by Kumar et al. [14]. Annealing for double the relaxation time at 623 K results in further embrittlement, which is not only caused by relaxation but also superimposed by partial crystallization. Hence, this marks the lower boundary for the annealing tests and is excluded from further analysis. Nevertheless, it is to mention that Vit105 still retains certain ductility despite partial crystallization (black curves), which underlines its excellent resistance against embrittlement and makes it one of the most promising alloys for industrial applications. The blue curves represent the rejuvenated specimens, which were first embrittled according to protocol 5 (see Fig. 1a), followed by a heat treatment in the supercooled liquid at 713 K with subsequent water quenching to obtain a glass with a high fictive temperature. The gain of about 2 % ductility by this rejuvenation procedure is indicated with a black arrow. Next to ductility, other characteristic values are also changing, such as the Young's modulus E that increases from 95 to 108 GPa with decreasing T_f. The evolution of $\sigma_y^{0.2\ \%}$, σ_f, E, ε_f and HV5 corresponding to the yield strength at 0.2 % strain, the fracture strength, the Young's modulus, the fracture strain and the Vickers hardness, respectively, of all investigated conditions are summarized in Table 2.

3.3. Structural changes as a function of T_f

Synchrotron diffraction experiments were performed for the as-cast and annealed samples (all annealing states from Fig. 1a). The structure factor S(Q) as well as the reduced PDF, G(r), for the different states are shown in Fig. 5. The most significant structural changes can be seen at the first and second sharp diffraction peak (FSDP and SSDP), which is mainly reflected in an increase in their intensity. Fourier transformation to the real space yields to the reduced PDF as shown in Fig. 5b, revealing changes on the short- and medium-range order (MRO). The detailed changes for the different fictive temperatures are shown in the insets as well as the difference plot in Fig. 5c, revealing primary alterations on the 1st, 2nd and 3rd coordination shell. The former corresponds to changes on the short-range order (SRO), whereas the 2nd and 3rd yield

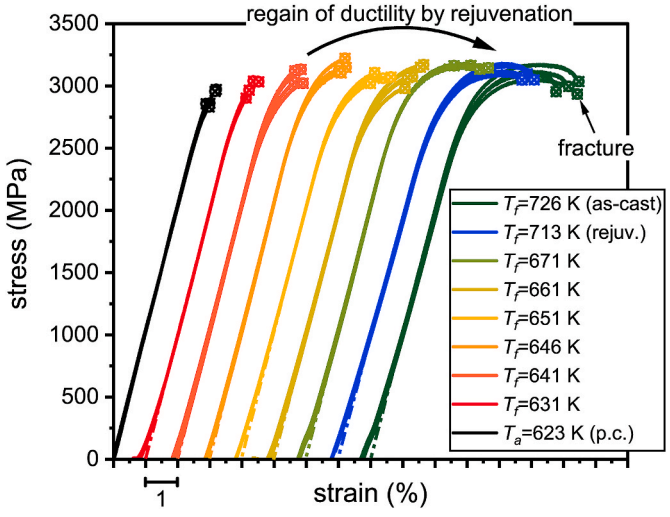

Fig. 4. Engineering stress-strain curves for different fictive temperatures T_f, revealing significant embrittlement with decreasing T_f. The deepest annealing temperature (T_a = 623 K, black curves) is affected by partial crystallization (p.c.) as revealed in DSC experiments.

Table 2
Summary of the mechanical parameters for the as-cast, rejuvenated and relaxed samples with the Youngs modulus E, the engineering yield strength $\sigma_y^{0.2\ \%}$ at 0.2 % strain, the fracture strength σ_f, the fracture strain ε_f and the Vickers hardness $HV5$.

Annealing temperature T_a (K)	$\sigma_y^{0.2\ \%}$ (GPa)	σ_f (GPa)	E (GPa)	ε_f (%)	Hardness $HV5$
– (As-cast)	2.79 ± 0.06	2.98 ± 0.04	95 ± 2	6.50 ± 0.26	522 ± 5
713	2.76 ± 0.03	3.07 ± 0.03	93 ± 2	5.91 ± 0.18	527 ± 2
671	2.83 ± 0.02	3.16 ± 0.06	98 ± 3	5.52 ± 0.29	529 ± 4
661	2.82 ± 0.03	3.12 ± 0.04	100 ± 1	4.59 ± 0.19	530 ± 4
651	2.87 ± 0.03	3.07 ± 0.03	98 ± 1	4.49 ± 0.25	533 ± 2
646	2.92 ± 0.09	3.18 ± 0.06	104 ± 3	4.28 ± 0.07	538 ± 2
641	2.86 ± 0.07	3.08 ± 0.05	102 ± 3	3.88 ± 0.13	547 ± 8
631	2.89 ± 0.04	3.13 ± 0.08	108 ± 2	3.45 ± 0.15	547 ± 6
623	2.85 ± 0.04	2.89 ± 0.06	103 ± 2	3.04 ± 0.12	553 ± 2

information on the MRO. Especially the 2nd coordination shell provides information on the interconnectivity of the clusters, specifically whether they share one (2 r_1), two ($\sqrt{2}$ r_1), three ($\sqrt{8/3}$ r_1) or four ($\sqrt{3}$ r_1) atoms. The position r_1 corresponds to the interatomic distance. However, the 1st peak of G(r) mainly consists of multiple contributions to the scattering factor S(Q). The contribution of the individual interatomic distances can be described by the Faber-Ziman weighting factor w_{ij} of the elemental pairs ij, which can be calculated via:

$$w_{ij} = (2 - \delta_{ij}) \frac{c_i c_j f_i f_j}{\left(\sum_i c_i f_i\right)^2} \tag{4}$$

with the concentration c_i, c_j (in at%) and atomic form factor f_i, f_j of the elements of i and j and the Kronecker delta δ_{ij} [51–53]. The weighting factor shown in Fig. 5b corresponds to the mean weighting factor of the measured Q-range, since w_{ij} is as the atomic form factor Q-dependent (more details in the SI). The shape of the first peak in G(r) is dominated by the Zr–Zr and Zr–Cu bond lengths, since these elements have the highest atomic form factor and contribute the most to the scattering signal. To determine a proper value for the interatomic distance, the first peak of G(r) is fitted with a Gaussian function (dotted line in Fig. 5b), which results in a mean value of the peak position of r_1 = 3.00 Å. This value is further used to calculate the distances resulting from the different cluster connection schemes, which are indicated with dotted-dashed lines. With respect to the cluster connection schemes, the predominant peak evolution occurs at the 3-atom connection around 4.9 Å, indicating an increase in neighboring clusters sharing 3 atoms. Less severe changes are observed for the 1-atom connection, whereas the length scale of the 4 and 2-atom connections stay rather unchanged.

3.4. Transfer to a BMG component

This extensive set of mechanical data for a wide range of fictive temperatures can be used in the following to determine the mechanical properties of a complex BMG component based only on the determination of T_f. For this purpose, a complex component was produced by die casting and segmented for analysis by DSC. This component can be of any shape though a watch bezel with typical features such as numerals was exemplarily chosen in this study as shown in Fig. 6a. The segmentation can be read like a dial, with the time corresponding to the respective analyzed position. The amorphous structure throughout the bezel was verified by X-ray diffraction and DSC experiments (not shown here, see SI). The latter reveals a constant crystallization enthalpy release of −3.4 kJ g-atom^{-1} throughout the bezel, which is on the same order of the as-cast beam specimen, proving that no crystallization occurred across the whole component. Since the fictive temperature is set due to the inherent cooling conditions of the casting process, a detailed analysis of the relaxation enthalpy release across the entire component yields information about the thermal history at each position

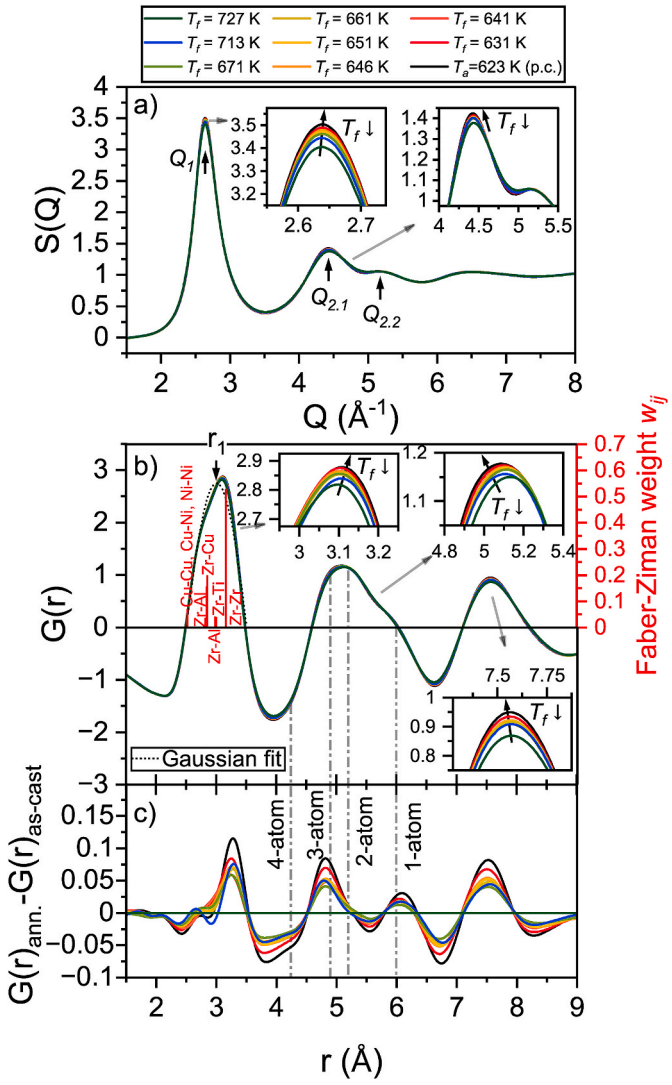

Fig. 5. a) Effect of the fictive temperature on the structure factor S(Q) of Vit105. The insets show a magnified view of the first two peaks, indicating mainly an increase in the peak intensity. b) shows the reduced pair distribution function G(r) of the same annealing states with insets of the first three peaks. The different bond lengths of the atomic pairs with their weighting factor w_{ij} are indicated based on the atomic radii reported in Ref. [54]. The largest contribution to the scattering signal comes from the Zr–Zr and Zr–Cu atomic pairs. All atomic pairs with a contribution below 1 % are not shown. The mean interatomic distance r_1 is determined based on the Gaussian fit of the first peak (dotted line). This value is used to determine the one, two, three and four atom connection (dotted-dashed lines). c) The difference in the reduced pair distribution function between the annealed and as-cast states shows the length scales at which the dominant structural changes occur.

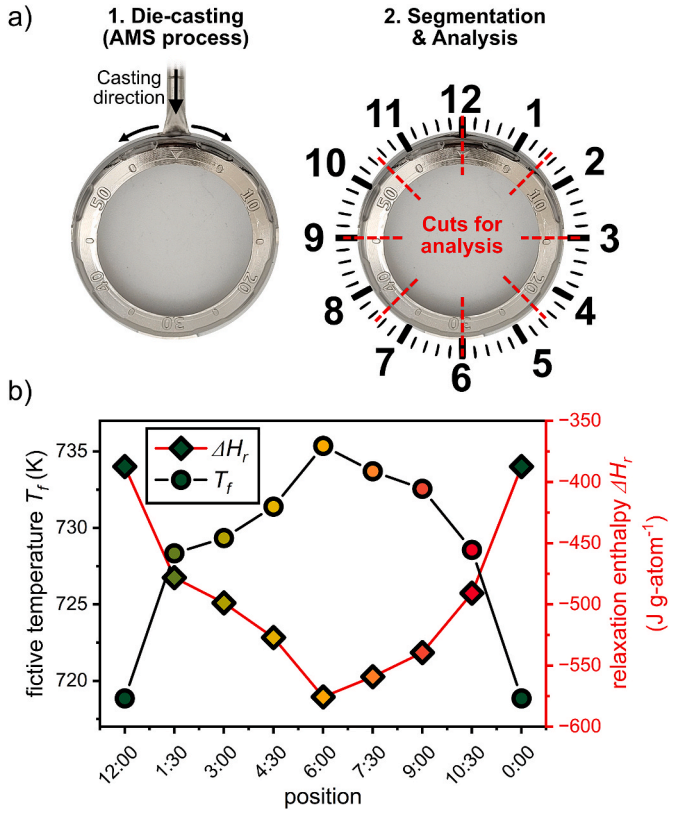

Fig. 6. a) Case study of a bezel component for watch applications. The bezel is segmented and thoroughly analyzed by DSC with b) showing the relaxation enthalpy across the bezel, which drastically changes from 12:00 (=0:00) o'clock (position of the feeder channel) to the 6:00 o'clock position. A larger absolute relaxation enthalpy release upon heating indicates a higher enthalpic state frozen-in during the casting process, which corresponds to a higher fictive temperature.

of the component. The results are shown in Fig. 6b, revealing a highly inhomogeneous relaxation state throughout the bezel. The evolution of the relaxation enthalpy can be directly related to the location of the feeder channel, since this is the position where the hot melt is injected into the cavity. This implies that the cooling rate at this position (12:00 = 0:00) is the slowest, while the opposite side (6:00) experiences the fastest cooling rate. Consequently, the relaxation states differ from the most relaxed at the feeder position to the least relaxed at the 6 o'clock position. This results in differing structural and enthalpic states, leading to an inhomogeneous distribution of the mechanical properties throughout the bezel. This course is well reflected by changes in the fictive temperature, i.e. the segment of the largest absolute relaxation enthalpy release exhibits the highest fictive temperature vice versa.

4. Discussion

Metallic glasses contain a significant amount of free volume in their structure, which is one of the most important structural features that influences the mechanical properties of amorphous alloys. It is well known that changes in the free volume are a simple way to describe the plastic deformation behavior of metallic glasses, as shown by the well-known models proposed by Spaepen [55] or Argon [56]. However, the evolution of free volume of metallic glasses is more difficult to quantify than the enthalpic state, which is a property directly accessible by calorimetric measurements. In general, both properties are usually correlated in the vicinity of the glass transition by the following linear equation [57,58]:

$$\Delta H_{l-x} = \beta' \bullet \nu_f \tag{5}$$

where ν_f is the change in free volume per atomic volume and β' is a proportionality constant, that can be interpreted as the formation energy of a vacancy with the magnitude of one atomic volume, which is discussed in detail in Ref. [57]. Since the enthalpy state is lowered upon thermal annealing as shown in Fig. 7a, the excess free volume must be likewise reduced according to Equation (5). These changes can be quantified in first approximation using the proportionality constant β' of the $Zr_{55}Cu_{30}Al_{10}Ni_5$ alloy, which is compositionally close to the studied Vit105 composition. Slipenyuk and Eckert [58] and Haruyama et al. [59] reported β' to be 552 kJ g-atom^{-1} and 718 kJ g-atom^{-1}, respectively, resulting in a mean value of β'=635 kJ g-atom^{-1}, which is used to estimate changes in the free volume, as shown on the right axis in Fig. 7a. This approximation is considered reasonable as the values are in

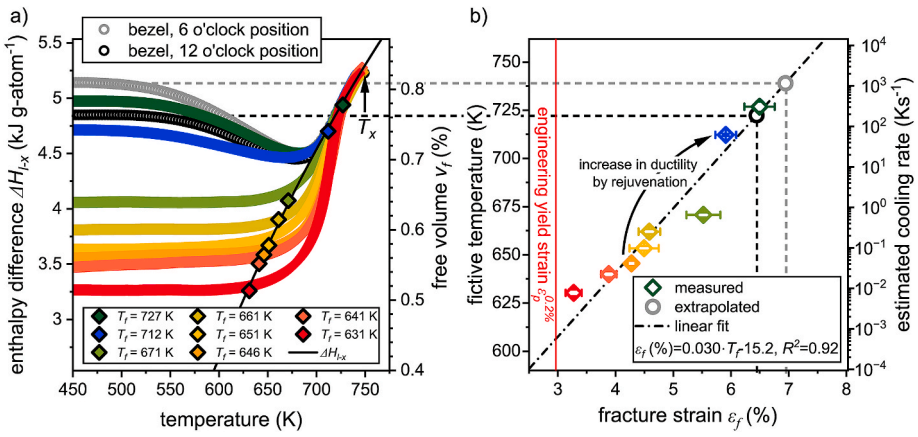

Fig. 7. a) Enthalpy difference $\Delta H_{l\text{-}x}$ as a function of temperature for different Vit105 structural states. The bezel segments at the positions of the highest and lowest fictive temperature are additionally shown. The right axis represents the free volume, which was calculated by using β' of a similar composition reported in Refs. [58, 59]. b) represents the bending strain to failure as a function of the fictive temperature, allowing the estimation of the mechanical properties of complex shaped components by a single DSC measurement based on the linear fit. The correlation of T_f and the cooling rate is additionally shown.

good agreement with other Zr-based bulk metallic glasses, such as $Zr_{44}Ti_{11}Ni_{10}Cu_{10}Be_{25}$ (Vit1b) with 623 kJ g-atom^{-1} [60]. Therefore, Zr-based BMGs seems to exhibit a fairly similar β' constant regardless of their composition. Hence, thermal annealing results in local structural ordering as can be seen from the structural data in Fig. 5, resulting in a reduction of deformation flow units by annihilation of excess free volume, which is responsible for the severe deterioration in the fracture strain as visible in Fig. 7b. This is further reflected in the observed mechanical hardening caused by relaxation (see Table 2).

On the other hand, plasticity can be remarkably recovered by the rejuvenation treatment, where T_f and ε_f is elevated from 641 K to 713 K and from 3.88 % up to 5.91 %, respectively. This is caused by reintroducing enthalpy as well as free volume into the system. The latter is supported by the mechanical softening from 547 HV5 (T_f = 641 K) to 527 HV5 (T_f = 713 K) as well as the structural data, where the FSDP of S (Q) reveals less intensity, i.e. less order after rejuvenation compared to the initial relaxed state. It is suggested that the formation of STZs as the initiator for shear band formation is restricted by relaxation to deeper T_f states, whereas it becomes easier by rejuvenation which induces free volume and disorder. Therefore, rejuvenation may lead to an increased number of STZ sites, which act as initiation and propagation of plastic deformation [61]. Furthermore, Pan et al. reported the volume of STZs to be crucial for the plastic flow behavior of BMGs, with larger STZ volumes facilitating the formation of multiple shear bands [62]. However, irrespective of the exact mechanism, the introduction of free volume and disorder by rejuvenation directly contributes to the significant improvement of plasticity and is expected to be applicable to other metallic glasses. Furthermore, the limited size of the supercooled liquid region is a restricting factor in achieving higher T_f values by conventional annealing. Additional rejuvenation requires processes such as cold rolling or high pressure torsion [26,38], which in turn undesirably alter the shape of the material. An alternative approach to maintain the sample geometry is cryogenic cycling, although it has been reported that this method rejuvenates samples only temporarily and loses its effect after a short period of time [38,63]. Therefore, structural rejuvenation by thermal annealing is a reliable and fast method for improving the properties of relaxed parts, with the only limitation in the size of the SCLR that usually does not allow to achieve a fictive temperature as high as in the as-cast condition.

The systematic correlation of the thermal history with the mechanical properties allows to characterize any amorphous component of Vit105 of any shape to be specified, simply by performing calorimetric measurements and determining its fictive temperature. This allows to characterize and estimate their mechanical properties, especially within a part that experienced different cooling rates at different positions due to inhomogeneous heat distribution, as shown for the 'bezel' component in Fig. 6. The enthalpy difference curves of the 6 and 12 o'clock position, which are the positions with the most significant difference in their fictive temperature, were exemplarily plotted in Fig. 7. These differences translate in an extrapolated bending strain to failure of 6.5 % and 7 % or calculated cooling rates of about 130 Ks^{-1} (T_f = 719 K) and 750 Ks^{-1} (T_f = 735 K), for the 6 and 12 o'clock position, respectively. The estimated cooling rates based on Equation (3) seem to be reasonable and comparable to data reported by Koziel et al. [64]. They analyzed the cellular spacing of a crystalline alloy during suction casting to determine the cooling rate as a function of the casting size, a technique typically used to produce BMGs. A corresponding cooling rate of 177 Ks^{-1} and 410 Ks^{-1} is reported for a 2 and 3 mm cylindrical rod, respectively [64]. This is in very good agreement with the estimated cooling rate of 313 Ks^{-1} for a beam with dimensions right in between (2 mm × 3 mm beams, T_f = 727 K). By utilizing the same formula for the deepest relaxation state that was fully amorphous (T_f = 631 K), the calculated (quasi-static) cooling rate of 0.01 Ks^{-1}, which is the equivalent cooling rate achieved after 133 h of annealing, translates to a hypothetical critical casting thickness of 32 cm [65]. This is way above the critical casting size of Vit105 (d_c~10 mm) as well as any known Zr-based metallic glass former [2,8,9]. Therefore, structural states with equivalent cooling rates that are below the critical cooling rate R_c (for instance: R_c of Vit105 is about 40 Ks^{-1} [9]) cannot be achieved by conventional casting processes due to crystallization, but only after annealing during post processing. This means that Vit105 will either be amorphous and ductile after casting or crystalline if the part is produced too thick.

It is well known that relaxation directly affects the atomic structure of the system. The underlying structural motif that is most dominant in Vit105 can be deduced from peak positions in S(Q) (see Fig. 5), specifically from the ratio of $Q_{2.1}/Q_1$ and $Q_{2.2}/Q_1$. Q_1 corresponds to the peak position of the first maximum and $Q_{2.1}$ and $Q_{2.2}$ to the two local maxima of the second peak, as it is composed of two subpeaks. An ideal icosahedral short-range order (ISRO) is observed when the ratio of the peak positions correspond to 1.71 and 2.04, respectively [48,66,67]. For Vit105, the ratio yields to similar values around 1.68 and 1.96 for all relaxation states, as changes are rather observed in the peak intensity and not the peak position. This indicates that the structural order is mainly dominated by icosahedra. The deviations of just 1.8 % and 3.9 % from the theoretical values indicates a slightly distorted ISRO in the glassy state [48,66], similar to the findings of Kelton et al. reporting distortions in the ISRO of a Zr–Ti–Ni composition [68]. Such an underlying ISRO is typical for Zr-based BMGs, as Zr atoms tend to form icosahedral-type polyhedral [69,70]. Changes within the MRO and their evolution with increasing temperature can be deduced from the FSDP of

the total structure factor, as shown in Fig. 8a and b for the peak height S(Q_1) and the corresponding full-width at half maximum (FWHM). Unless structural relaxation takes place, the observed changes in S(Q) (e.g. decrease in the peak height or increase in the FWHM) with increasing temperature are rather small and can be attributed to atomic vibrations, which can be described within the Debye theory [71,72]. The severe changes that are visible at elevated temperatures of about 625 K for the as-quenched glass (increase in S(Q_1) and decrease in FWHM Q_1) represents structural relaxation into deeper energy states as the high cooling rates during casting led to a high fictive temperature. Similar behavior is visible for the rejuvenated specimen that also vitrified with a high fictive temperature. Such a structural ordering is less (or not) visible upon heating for the relaxed samples with fictive temperatures below 700 K, as the calculated cooling rate during vitrification (see Table 1) is slower than the applied heating rate of 0.33 Ks^{-1}. This implies that relaxation processes associated with the timescales that can be probed with this heating rate already occurred. Interestingly, minor relaxation processes, best visible in the FWHM of the FSDP in Fig. 8b (e.g. light green curve, T_f = 671 K), are still occurring at temperatures close to T_g, despite being 'fully' relaxed to the equilibrium liquid at long timescales. This indicates that there are a certain number of structures (likely the one containing the larger atoms) that are still not fully relaxed into the metastable equilibrium and thus are able to further relax in a subsequent heating process. Once T_g is reached, all curves start to align with each other independent of the thermal history as the structure in the equilibrium liquid at a respective temperature is the same. Fig. 8c and d shows the change of S(Q_1) and the FWHM(Q_1) at 300 K as a function of the fictive temperature. The correlation plot of both parameters with the bending strain to failure is provided in the insets of the respective diagram with a high correlation (R^2 of 0.89 and 0.93) of the systems ductility with structural features of the FSDP. An increase in S(Q_1), which goes hand in hand with a narrowing of the peak, represents changes on the MRO length scale of the system towards a more ordered icosahedral structure.

A more convenient description of the structure is provided by the reduced PDF, G(r), which describes the structure in real space instead of the reciprocal space. For a more quantitative analysis, the changes in ductility as a function of the annealing state, more precisely the fictive temperature of Vit105 is correlated to various parameters of G(r), such as the peak height representing the probability distribution of structural motifs at a respective length scale [73]. As indicated in Fig. 9a, changes can be observed across the nearest neighbors (SRO), the atom connections as well as the MRO length scale, which are quantified in detail in Fig. 9b. Since Zr is the main constituent of Vit105, Zr atoms are primarily coordinated around Ni and Cu atoms for icosahedral clusters, as supported by MD simulations of similar Zr-based alloys in Refs. [70,74]. Therefore, the inter-cluster atomistic rearrangements during relaxation primarily took place for Zr, as visible for the SRO in the form of a predominant increase in the peak height of G(r = 3.16 Å), representing an increase of the Zr–Zr atomic pair. This structural ordering at the SRO is further mirrored by an increasing 3-atom connection denoted as G(r = $\sqrt{8/3}$ r_1) (=amplitude of G(r) at the length scale of r = $\sqrt{8/3}$ r_1), which is not surprising as icosahedral clusters consist of 20 triangular faces, facilitating this face-sharing connection [75]. A similar opposing trend of decreasing ductility with increasing atom connection was already observed in a previous study for Pt/Pd-based metallic glasses [49]. Moreover, simulations of Ding et al. have shown that the face-sharing (3-atom) connection is the stiffest connection and therefore least able to accommodate shear strain [75]. Hence, this connection seems to play a distinctive role in the deformation mechanism by structural aging or in other words the degree of relaxation. However, it is to mention that the deformation mechanism is a complex phenomenon in multicomponent glass forming alloys that is not only affected by cluster connections, but also by the SRO and MRO, which defines the distribution of free volume [76]. Therefore, it is not possible to predict the ductility by just analyzing the 3-atom connection as the deformation mechanism is too complex to deduce it to a single parameter. This is visible upon analyzing the correlation length ξ, which essentially describes the degree of order present in a system. The parameter ξ can be deduced from the exponential decay (f(r) = A·exp(-r/ξ)) of the peak heights in G(r) (details in the SI), yielding insights to length scales beyond the nearest neighbors or cluster connections. In general, a larger correlation length ξ indicates a more ordered atomic arrangement over longer distances [77,

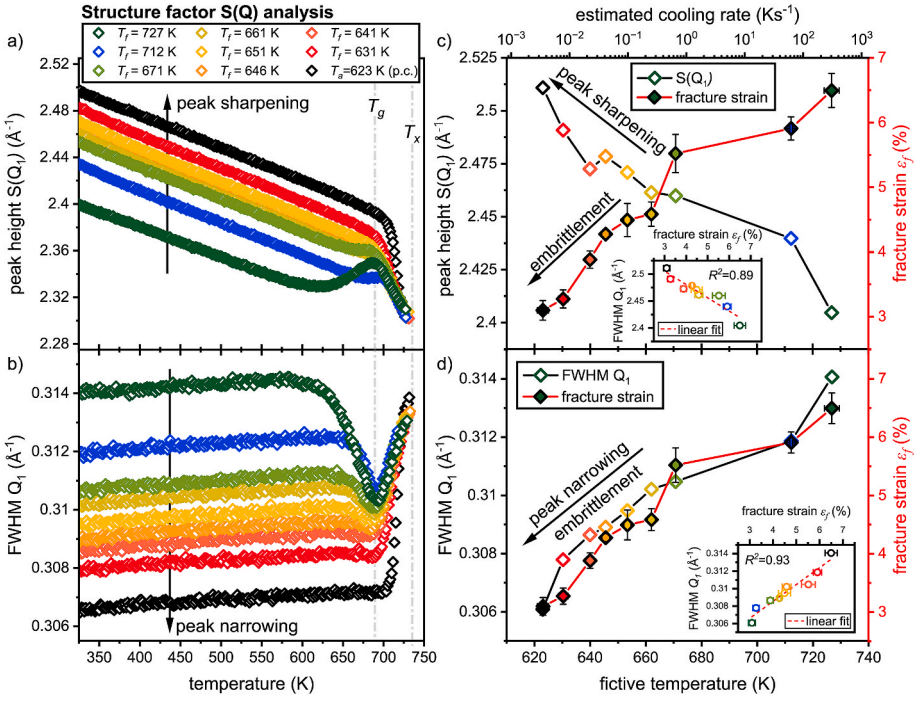

Fig. 8. Evolution of a) the peak height S(Q_1) and b) the full-width at half maximum FWHM Q_1 of the first sharp diffraction peak Q_1 upon heating with 0.33 Ks^{-1} measured in an in-situ high energy synchrotron X-ray diffraction experiment. c) and d) show the evolution of S(Q_1) and FWHM Q_1 at 300 K, respectively, as a function of the fictive temperature with a high correlation of R^2 of 0.89 and 0.93 as shown in the insets.

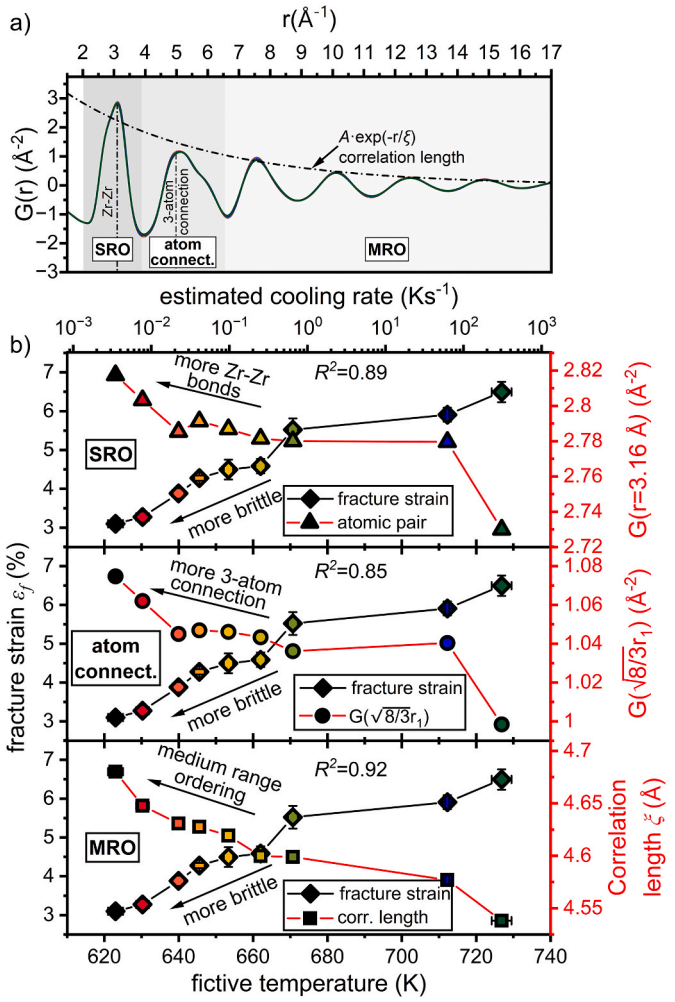

Fig. 9. a) Overview of the analyzed length scales from the short-range order over the atom connections to the medium-range order of all Vit105 annealing states. b) The fracture strain as a measure of ductility is shown along the evolution of the Zr–Zr atomic pair (SRO), the absolute value of the 3-atom connection G($\sqrt{8/3}$ r$_1$) as well as the correlation length ξ (MRO) at 300 K, as a function of the fictive temperature. In general, structural ordering can be observed at all length scales, correlating well with the decrease in ductility as fictive temperature decreases. The given R^2 corresponds to the correlation of the fracture strain with the respective parameter.

78], i.e. that the observed local rearrangement of the atoms (SRO and cluster connections) continues up to the MRO length scale. In summary, structural aging causes changes over a wide range of length scales (SRO, atom connections and MRO), indicating that the loss of free volume is associated with an ordering towards a more icosahedral ordered structure. An increased number of closed-packed icosahedral motifs results in more 'densely packed' regions with a lower degree of free volume [79, 80]. Consequently, the formation of STZs and ultimately shear bands is restricted, as such a structure is less capable of accommodating shear strain [13,56], resulting in the progressive embrittlement as the fictive temperatures decreases.

5. Conclusion

To conclude, the mechanical properties as a function of the intrinsic enthalpic state of the Vit105 alloy was characterized for the as-cast as well as various relaxation and rejuvenation states, covering a broad range that has not been systematically studied so far. The annealing-induced embrittlement can be described by the fictive temperature, resembling the internal structure of the system. HEXRD studies revealed that the structure is dominated by icosahedral motifs that are forming an icosahedral short-range order. Furthermore, annealing results not only in an ordering on the short- but also the medium-range order. Specifically, the increasing trend in the reduced pair distribution function on the length scale of rigid 3-atom cluster connections were found to be decisive for the ductility of the system. Additionally, it was shown that complex BMG parts exhibit highly inhomogeneous relaxation states distributed throughout the entire component. This complicates the measurement of the macroscopic mechanical properties even more. Therefore, we propose a rather simple characterization technique of complex components with a complex thermal history using only calorimetry, allowing a profound estimation of the mechanical performance at any point of the cast component based on the intrinsic enthalpic state.

CRediT authorship contribution statement

Lucas M. Ruschel: Writing – original draft, Visualization, Validation, Supervision, Project administration, Methodology, Investigation, Formal analysis, Data curation, Conceptualization. **Sergej Jakovlev:** Writing – review & editing, Validation, Methodology, Investigation, Formal analysis, Data curation. **Oliver Gross:** Writing – review & editing, Visualization, Resources, Investigation, Data curation, Conceptualization. **Nico Neuber:** Writing – review & editing, Methodology, Funding acquisition, Formal analysis. **Bastian Adam:** Writing – review & editing, Project administration, Investigation, Data curation. **Maximilian Frey:** Writing – review & editing, Investigation, Data curation. **Benedikt Schmidt:** Writing – review & editing, Investigation, Data curation. **Benedikt Bochtler:** Writing – review & editing, Resources. **Ralf Busch:** Writing – review & editing, Supervision, Project administration, Funding acquisition.

Declaration of competing interest

The authors declare the following financial interests/personal relationships which may be considered as potential competing interests: Ralf Busch reports equipment, drugs, or supplies was provided by Heraeus AMLOY Technologies GmbH. Ralf Busch reports financial support was provided by Federal Ministry for Economic Affairs and Climate Action. If there are other authors, they declare that they have no known competing financial interests or personal relationships that could have appeared to influence the work reported in this paper.

Data availability

Data will be made available on request.

Acknowledgements

This research was conducted and funded in collaboration with Heraeus AMLOY Technologies GmbH. They also supplied the raw elements to produce the alloys. This research was also financially supported by the German Federal Ministry for Economic Affairs and Climate Action (BMWK) under the IGF program (project no. AiF-IGF 21469N2). The members of the industrial user committee and colleagues from the 'fem – Forschungsinstitut Edelmetalle + Metallchemie' are acknowledged for their contribution to this work as well. We would also like to thank Marie Erbeia for her contribution as part of her master's thesis and for her watchmaking expertise as well as Isabella Gallino for many fruitful discussions. We acknowledge DESY (Hamburg, Germany), a member of the Helmholtz Association HGF, for the provision of experimental facilities. Parts of this research were carried out at PETRA III and we would like to thank Ulrich Lienert and Zoltan Hegedüs for assistance in using the P21.2 beam facility. Furthermore, we'd like to thank Valeria Lemkova and Fabian Vollmers who assisted during the campaign. Beamtime was allocated for proposal I-20231426.

Appendix A. Supplementary data

Supplementary data to this article can be found online at https://doi.org/10.1016/j.mtadv.2024.100522.

References

[1] W. Klement, R. Willens, P. Duwez, Non-crystalline structure in solidified gold–silicon alloys, Nature 187 (4740) (Sep. 1960) 869–870, https://doi.org/10.1038/187869b0.

[2] A.L. Greer, E. Ma, Bulk metallic glasses: at the cutting edge of metals research, MRS Bull. 32 (8) (2007) 611–619, https://doi.org/10.1557/mrs2007.121.

[3] L.M. Ruschel, et al., Ni-Nb-P-based bulk glass-forming alloys: superior material properties combined in one alloy family, Acta Mater. 253 (January) (Jul. 2023) 118968, https://doi.org/10.1016/j.actamat.2023.118968.

[4] H. Jiang, et al., Effect of sulfur on the glass-forming ability, phase transformation, and thermal stability of Cu-Zr-Al bulk metallic glass, Acta Mater. 212 (Jun. 2021) 116923, https://doi.org/10.1016/j.actamat.2021.116923.

[5] J. Shen, Q. Chen, J. Sun, H. Fan, G. Wang, Exceptionally high glass-forming ability of an FeCoCrMoCBY alloy, Appl. Phys. Lett. 86 (15) (2005) 151907, https://doi.org/10.1063/1.1897426.

[6] N. Neuber, et al., The role of Ga addition on the thermodynamics, kinetics, and tarnishing properties of the Au-Ag-Pd-Cu-Si bulk metallic glass forming system, Acta Mater. 165 (2019) 315–326, https://doi.org/10.1016/j.actamat.2018.11.052.

[7] A.J. Drehman, A.L. Greer, D. Turnbull, Bulk formation of a metallic glass: Pd40Ni40P20, Appl. Phys. Lett. 41 (8) (1982) 716–717, https://doi.org/10.1063/1.93645.

[8] M. Telford, The case for bulk metallic glass, Mater. Today 7 (3) (2004) 36–43, https://doi.org/10.1016/S1369-7021(04)00124-5.

[9] X. Lin, Bulk Glass Formation and Crystallization of Zr-Ti Based Alloys, California Institute of Technology (Caltech), 1997. Dissertation.

[10] M.L. Morrison, et al., Four-point-bending-fatigue behavior of the Zr-based Vitreloy 105 bulk metallic glass, Mater. Sci. Eng. A 467 (1–2) (Oct. 2007) 190–197, https://doi.org/10.1016/j.msea.2007.05.066.

[11] G. Kumar, T. Ohkubo, K. Hono, Effect of melt temperature on the mechanical properties of bulk metallic glasses, J. Mater. Res. 24 (7) (Jul. 2009) 2353–2360, https://doi.org/10.1557/jmr.2009.0272.

[12] Y.Q. Cheng, E. Ma, Atomic-level structure and structure–property relationship in metallic glasses, Prog. Mater. Sci. 56 (4) (May 2011) 379–473, https://doi.org/10.1016/j.pmatsci.2010.12.002.

[13] C. Schuh, T. Hufnagel, U. Ramamurty, Mechanical behavior of amorphous alloys, Acta Mater. 55 (12) (2007) 4067–4109, https://doi.org/10.1016/j.actamat.2007.01.052.

[14] G. Kumar, P. Neibecker, Y.H. Liu, J. Schroers, Critical fictive temperature for plasticity in metallic glasses, Nat. Commun. 4 (2013), https://doi.org/10.1038/ncomms2546.

[15] J. Ketkaew, et al., Mechanical glass transition revealed by the fracture toughness of metallic glasses, Nat. Commun. 9 (1) (Aug. 2018) 3271, https://doi.org/10.1038/s41467-018-05682-8.

[16] Y. Zhao, et al., Ultrastable metallic glass by room temperature aging, Sci. Adv. 8 (33) (Aug. 2022) 1–9, https://doi.org/10.1126/sciadv.abn3623.

[17] C.T. Moynihan, A. Easteal, M.A. Bolt, J. Tucker, Dependence of the fictive temperature of glass on cooling rate, J. Am. Ceram. Soc. 59 (1–2) (Jan. 1976) 12–16, https://doi.org/10.1111/j.1151-2916.1976.tb09376.x.

[18] A.R. Yavari, J.J. Lewandowski, J. Eckert, Mechanical properties of bulk metallic glasses, MRS Bull. 32 (8) (2007) 635–638, https://doi.org/10.1557/mrs2007.125.

[19] T.-W. Wu, F. Spaepen, The relation between enbrittlement and structural relaxation of an amorphous metal, Philos. Mag. B 61 (4) (Apr. 1990) 739–750, https://doi.org/10.1080/13642819008219307.

[20] P. Murali, U. Ramamurty, Embrittlement of a bulk metallic glass due to sub-annealing, Acta Mater. 53 (5) (Mar. 2005) 1467–1478, https://doi.org/10.1016/j.actamat.2004.11.040.

[21] G. Kumar, D. Rector, R.D. Conner, J. Schroers, Embrittlement of Zr-based bulk metallic glasses, Acta Mater. 57 (12) (Jul. 2009) 3572–3583, https://doi.org/10.1016/j.actamat.2009.04.016.

[22] W.H. Jiang, F.X. Liu, H. Choo, P.K. Liaw, Effect of structural relaxation on mechanical behavior of a Zr-based bulk-metallic glass, Mater. Trans. 48 (7) (2007) 1781–1784, https://doi.org/10.2320/matertrans.MJ200734.

[23] Y. Sun, A. Concustell, A.L. Greer, Thermomechanical processing of metallic glasses: extending the range of the glassy state, Nat. Rev. Mater. 1 (9) (Jun. 2016) 16039, https://doi.org/10.1038/natrevmats.2016.39.

[24] B. Jessen, E. Woldt, Stored energy of the deformed metallic glass Ni78Si8B14, Thermochim. Acta 151 (C) (Sep. 1989) 179–186, https://doi.org/10.1016/0040-6031(89)85347-X.

[25] S. Scudino, K.B. Surreddi, J. Eckert, Mechanical properties of cold-rolled Zr60Ti5Ag5Cu12.5Ni10Al7.5 metallic glass, Phys. status solidi 207 (5) (May 2010) 1118–1121, https://doi.org/10.1002/pssa.200983366.

[26] C. Wang, et al., High stored energy of metallic glasses induced by high pressure, Appl. Phys. Lett. 110 (11) (Mar. 2017) 1–5, https://doi.org/10.1063/1.4978600.

[27] C. Ebner, B. Escher, C. Gammer, J. Eckert, S. Pauly, C. Rentenberger, Structural and mechanical characterization of heterogeneities in a CuZr-based bulk metallic glass processed by high pressure torsion, Acta Mater. 160 (Nov. 2018) 147–157, https://doi.org/10.1016/j.actamat.2018.08.032.

[28] F. Meng, K. Tsuchiya, Seiichiro, Y. Yokoyama, Reversible transition of deformation mode by structural rejuvenation and relaxation in bulk metallic glass, Appl. Phys. Lett. 101 (12) (Sep. 2012) 121914, https://doi.org/10.1063/1.4753998.

[29] N. Adachi, Y. Todaka, Y. Yokoyama, M. Umemoto, Cause of hardening and softening in the bulk glassy alloy Zr50Cu40Al10 after high-pressure torsion, Mater. Sci. Eng. A 627 (Mar. 2015) 171–181, https://doi.org/10.1016/j.msea.2014.12.101.

[30] P. Denis, C.M. Meylan, C. Ebner, A.L. Greer, M. Zehetbauer, H.-J. Fecht, Rejuvenation decreases shear band sliding velocity in Pt-based metallic glasses, Mater. Sci. Eng. A 684 (October 2016) (Jan. 2017) 517–523, https://doi.org/10.1016/j.msea.2016.12.075.

[31] C.M. Meylan, J. Orava, A.L. Greer, Rejuvenation through plastic deformation of a La-based metallic glass measured by fast-scanning calorimetry, J. Non-Cryst. Solids X 8 (June) (Dec. 2020) 100051, https://doi.org/10.1016/j.nocx.2020.100051.

[32] K. Sun, et al., Structural rejuvenation and relaxation of a metallic glass induced by ion irradiation, Scr. Mater. 180 (Apr. 2020) 34–39, https://doi.org/10.1016/j.scriptamat.2020.01.023.

[33] P. Wang, M. Li, B. Malomo, L. Yang, Neutron irradiation-induced rejuvenation in ZrCu metallic glass, J. Mater. Sci. 57 (26) (Jul. 2022) 12642–12652, https://doi.org/10.1007/s10853-022-07446-8.

[34] T.C. Hufnagel, Cryogenic rejuvenation, Nat. Mater. 14 (9) (Sep. 2015) 867–868, https://doi.org/10.1038/nmat4394.

[35] W. Guo, R. Yamada, J. Saida, Rejuvenation and plasticization of metallic glass by deep cryogenic cycling treatment, Intermetallics 93 (August 2017) (Feb. 2018) 141–147, https://doi.org/10.1016/j.intermet.2017.11.015.

[36] S.V. Ketov, et al., Rejuvenation of metallic glasses by non-affine thermal strain, Nature 524 (7564) (Aug. 2015) 200–203, https://doi.org/10.1038/nature14674.

[37] T.J. Lei, et al., Microscopic characterization of structural relaxation and cryogenic rejuvenation in metallic glasses, Acta Mater. 164 (Feb. 2019) 165–170, https://doi.org/10.1016/j.actamat.2018.10.036.

[38] C.M. Meylan, et al., Stimulation of shear-transformation zones in metallic glasses by cryogenic thermal cycling, J. Non-Cryst. Solids 548 (June) (Nov. 2020) 120299, https://doi.org/10.1016/j.jnoncrysol.2020.120299.

[39] J. Ketkaew, et al., The effect of thermal cycling on the fracture toughness of metallic glasses, Acta Mater. 184 (Feb. 2020) 100–108, https://doi.org/10.1016/j.actamat.2019.11.046.

[40] M. Wakeda, J. Saida, J. Li, S. Ogata, Controlled rejuvenation of amorphous metals with thermal processing, Sci. Rep. 5 (1) (May 2015) 10545, https://doi.org/10.1038/srep10545.

[41] J. Saida, R. Yamada, M. Wakeda, S. Ogata, Thermal rejuvenation in metallic glasses, Sci. Technol. Adv. Mater. 18 (1) (Dec. 2017) 152–162, https://doi.org/10.1080/14686996.2017.1280369.

[42] S. Küchemann, et al., Energy storage in metallic glasses via flash annealing, Adv. Funct. Mater. 28 (50) (Dec. 2018) 1–9, https://doi.org/10.1002/adfm.201805385.

[43] W. Guo, T. Niiyama, R. Yamada, M. Wakeda, J. Saida, Synthesis and mechanical properties of highly structure-controlled Zr-based metallic glasses by thermal rejuvenation technique, J. Phys. Condens. Matter 35 (15) (Apr. 2023) 154004, https://doi.org/10.1088/1361-648X/acb8a0.

[44] Amorphous Metal Solutions GmbH (AMS).” https://ams-metal.de/.

[45] B. Bochtler, Thermophysical and Structural Investigations of a CuTi- and a Zr-Based Bulk Metallic Glass, the Influence of Minor Additions, and the Relation to Thermoplastic Forming, Saarland University, 2019.

[46] G. Ashiotis, et al., The fast azimuthal integration Python library: pyFAI, J. Appl. Crystallogr. 48 (2) (2015) 510–519, https://doi.org/10.1107/S1600576715004306.

[47] X. Qiu, J.W. Thompson, S.J.L. Billinge, PDFgetX2 : a GUI-driven program to obtain the pair distribution function from X-ray powder diffraction data, J. Appl. Crystallogr. 37 (4) (2004) 678, https://doi.org/10.1107/S0021889804011744, 678.

[48] O. Gross, et al., Signatures of structural differences in Pt–P- and Pd–P-based bulk glass-forming liquids, Commun. Phys. 2 (1) (Dec. 2019) 83, https://doi.org/10.1038/s42005-019-0180-2.

[49] N. Neuber, et al., Effect of composition and thermal history on deformation behavior and cluster connections in model bulk metallic glasses, Sci. Rep. 12 (1) (Oct. 2022) 17133, https://doi.org/10.1038/s41598-022-20938-6.

[50] M. Frey, et al., Laser powder bed fusion of Cu-Ti-Zr-Ni bulk metallic glasses in the Vit101 alloy system, Addit. Manuf. 66 (Mar. 2023) 103467, https://doi.org/10.1016/j.addma.2023.103467.

[51] T.E. Faber, J.M. Ziman, A theory of the electrical properties of liquid metals, Philos. Mag. A 11 (109) (Jan. 1965) 153–173, https://doi.org/10.1080/14786436508211931.

[52] T. Egami, S.J.L. Billinge, UNDERNEATH the BRAGG PEAKS Structural Analysis of Complex Materials, second ed., vol. 16, 2012.

[53] M.E. Stiehler, et al., The effect of Ni or Co additions on the structure of Zr60Cu30Al10 bulk metallic glass revealed by high-energy synchrotron radiation, Mater. Today Commun. 31 (April) (Jun. 2022) 103531, https://doi.org/10.1016/j.mtcomm.2022.103531.

[54] K.J. Laws, D.B. Miracle, M. Ferry, A predictive structural model for bulk metallic glasses, Nat. Commun. 6 (1) (2015) 8123, https://doi.org/10.1038/ncomms9123.

[55] F. Spaepen, A microscopic mechanism for steady state inhomogeneous flow in metallic glasses, Acta Metall. 25 (4) (1977) 407–415, https://doi.org/10.1016/0001-6160(77)90232-2.

[56] A. Argon, Plastic deformation in metallic glasses, Acta Metall. 27 (1) (1979) 47–58, https://doi.org/10.1016/0001-6160(79)90055-5.

[57] A. van den Beukel, J. Sietsma, The glass transition as a free volume related kinetic phenomenon, Acta Metall. Mater. 38 (3) (Mar. 1990) 383–389, https://doi.org/10.1016/0956-7151(90)90142-4.
[58] A. Slipenyuk, J. Eckert, Correlation between enthalpy change and free volume reduction during structural relaxation of Zr55Cu30Al10Ni5 metallic glass, Scr. Mater. 50 (1) (Jan. 2004) 39–44, https://doi.org/10.1016/j.scriptamat.2003.09.038.
[59] O. Haruyama, K. Kisara, A. Yamashita, K. Kogure, Y. Yokoyama, K. Sugiyama, Characterization of free volume in cold-rolled Zr55Cu30Ni5Al10 bulk metallic glasses, Acta Mater. 61 (9) (May 2013) 3224–3232, https://doi.org/10.1016/j.actamat.2013.02.010.
[60] Z. Evenson, R. Busch, Equilibrium viscosity, enthalpy recovery and free volume relaxation in a Zr44Ti11Ni10Cu10Be25 bulk metallic glass, Acta Mater. 59 (11) (Jun. 2011) 4404–4415, https://doi.org/10.1016/j.actamat.2011.03.064.
[61] F. Meng, K. Tsuchiya, M.J. Kramer, R.T. Ott, Reduction of shear localization through structural rejuvenation in Zr–Cu–Al bulk metallic glass, Mater. Sci. Eng. A 765 (July) (2019), https://doi.org/10.1016/j.msea.2019.138304.
[62] D. Pan, A. Inoue, T. Sakurai, M.W. Chen, Experimental characterization of shear transformation zones for plastic flow of bulk metallic glasses, Proc. Natl. Acad. Sci. 105 (39) (Sep. 2008) 14769–14772, https://doi.org/10.1073/pnas.0806051105.
[63] M.B. Costa, et al., Anelastic-like nature of the rejuvenation of metallic glasses by cryogenic thermal cycling, Acta Mater. 244 (May 2022) (Jan. 2023) 118551, https://doi.org/10.1016/j.actamat.2022.118551.
[64] T. Kozieł, K. Pajor, Ł. Gondek, Cooling rate evaluation during solidification in the suction casting process, J. Mater. Res. Technol. 9 (6) (Nov. 2020) 13502–13508, https://doi.org/10.1016/j.jmrt.2020.09.082.
[65] X.H. Lin, W.L. Johnson, Formation of Ti–Zr–Cu–Ni bulk metallic glasses, J. Appl. Phys. 78 (11) (Dec. 1995) 6514–6519, https://doi.org/10.1063/1.360537.
[66] S. Sachdev, D.R. Nelson, Theory of the structure factor of metallic glasses, Phys. Rev. Lett. 53 (20) (Nov. 1984) 1947–1950, https://doi.org/10.1103/PhysRevLett.53.1947.
[67] K.F. Kelton, et al., First X-ray scattering studies on electrostatically levitated metallic liquids: demonstrated influence of local icosahedral order on the nucleation barrier, Phys. Rev. Lett. 90 (19) (May 2003) 195504, https://doi.org/10.1103/PhysRevLett.90.195504.
[68] K.F. Kelton, A.K. Gangopadhyay, T.H. Kim, G.W. Lee, A case for local icosahedral order in undercooled metallic liquids and the influence on the nucleation barrier, J. Non-Cryst. Solids 352 (50–51) (Dec. 2006) 5318–5324, https://doi.org/10.1016/j.jnoncrysol.2006.08.009.
[69] T. Fukunaga, et al., Voronoi analysis of the structure of Ni-Zr-Al ternary metallic glass, Mater. Transacitions 48 (7) (2007) 1698–1702, https://doi.org/10.2320/matertrans.MJ200750.
[70] A. Takeuchi, K. Yubuta, M. Ogata, A. Inoue, Molecular dynamics simulations of critically percolated, cluster-packed structure in Zr–Al–Ni bulk metallic glass, J. Mater. Sci. 45 (18) (Sep. 2010) 4898–4905, https://doi.org/10.1007/s10853-010-4344-4.
[71] S. Sinha, P.L. Srivastava, R.N. Singh, Temperature-dependent structure and electrical transport in liquid metals, J. Phys. Condens. Matter 1 (9) (Mar. 1989) 1695–1705, https://doi.org/10.1088/0953-8984/1/9/014.
[72] N.A. Mauro, A.J. Vogt, M.L. Johnson, J.C. Bendert, K.F. Kelton, Anomalous structural evolution in Cu50Zr50 glass-forming liquids, Appl. Phys. Lett. 103 (2) (Jul. 2013), https://doi.org/10.1063/1.4813389.
[73] T. Egami, S.J. Billinge, Underneath the Bragg Peaks, first ed., vol. 7, Pergamon, Oxford, 2003 https://doi.org/10.1016/S1369-7021(03)00635-7.
[74] M. Celtek, S. Sengul, U. Domekeli, Glass formation and structural properties of Zr50Cu50-xAlx bulk metallic glasses investigated by molecular dynamics simulations, Intermetallics 84 (May 2017) 62–73, https://doi.org/10.1016/j.intermet.2017.01.001.
[75] J. Ding, E. Ma, M. Asta, R.O. Ritchie, Second-nearest-neighbor correlations from connection of atomic packing motifs in metallic glasses and liquids, Sci. Rep. 5 (1) (2015) 17429, https://doi.org/10.1038/srep17429.
[76] M.M. Trexler, N.N. Thadhani, Mechanical properties of bulk metallic glasses, Prog. Mater. Sci. 55 (8) (Nov. 2010) 759–839, https://doi.org/10.1016/j.pmatsci.2010.04.002.
[77] D. Ma, A.D. Stoica, X.-L. Wang, Power-law scaling and fractal nature of medium-range order in metallic glasses, Nat. Mater. 8 (1) (Jan. 2009) 30–34, https://doi.org/10.1038/nmat2340.
[78] H.-R. Jiang, et al., On the devitrification of Cu–Zr–Al alloys: solving the apparent contradiction between polymorphic liquid-liquid transition and phase separation, Acta Mater. 226 (Mar. 2022) 117668, https://doi.org/10.1016/j.actamat.2022.117668.
[79] Z.W. Zhu, et al., Relation between icosahedral short-range ordering and plastic deformation in Zr–Nb–Cu–Ni–Al bulk metallic glasses, Acta Mater. 59 (7) (Apr. 2011) 2814–2822, https://doi.org/10.1016/j.actamat.2011.01.020.
[80] L.M. Ruschel, et al., Development and optimization of novel sulfur-containing Ti-based bulk metallic glasses and the correlation between primarily crystallizing phases, thermal stability and mechanical properties, J. Alloys Compd. 960 (Oct. 2023) 170614, https://doi.org/10.1016/j.jallcom.2023.170614.